ACS APPLIED MATERIALS & INTERFACES

Research Article

www.acsami.org

# Novel Anodization Technique Using a Block Copolymer Template for Nanopatterning of Titanium Implant Surfaces

Terje Sjöström,*[,†] Laura E. McNamara,[‡] Li Yang,[§] Matthew J. Dalby,[‡] and Bo Su[†]

[†]School of Oral and Dental Sciences, University of Bristol, Bristol BS1 2LY, United Kingdom

[‡]Centre for Cell Engineering, University of Glasgow, Glasgow G12 8QQ, United Kingdom

[§]Analytical Science Division, National Physical Laboratory, Teddington, Middlesex TW11 0LW, United Kingdom

**ABSTRACT:** Precise surface nanopatterning is a promising route for predictable control of cellular behavior on biomedical materials. There is currently a gap in taking such precision engineered surfaces from the laboratory to clinically relevant implant materials such as titanium (Ti). In this work, anodization of Ti surfaces was performed in combination with block copolymer templates to create highly ordered and tunable oxide nanopatterns. Secondary ion mass spectroscopy (SIMS) and X-ray photoelectron spectroscopy (XPS) analyses showed that the composition of the anodized structures was mainly titania with small amounts of nitrogen left from the block copolymer. It was further demonstrated that these nanopatterns can be superimposed on more complex shaped Ti surfaces such as microbeads, using the same technique. Human mesenchymal stem cells were cultured on Ti microbead surfaces, with and without nanopatterns, in vitro to study the effect of nanotopography on Ti surfaces. The results presented in this work demonstrate a promising method of producing highly defined and well-arranged surface nanopatterns on Ti implant surfaces.

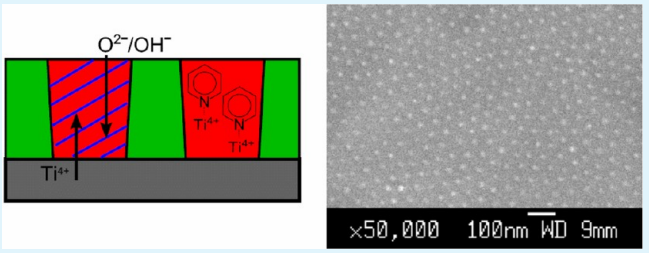


**KEYWORDS:** *nanopatterning, biomaterials, titanium, stem cells, block copolymers, anodization*

## 1. INTRODUCTION

Titanium is an important material for a range of applications including biomedical prostheses. Surface modification of Ti implants is an active area of research with great potential to improve the performance and lifetime of orthopedic implants. The last decades have seen developments in our understanding of the influence of surface topography on the biological response at implant surfaces, and specifically, it has become apparent that the surface topography at the nanoscale can have a major impact on protein adsorption,[1] cell behavior,[2] bacterial interactions,[3] and ultimately the integration of the implant into the host tissue.[4] Strikingly, it has been shown that cell signaling can change dramatically with small alterations in the dimension or arrangement of well-defined nanopatterns.[1,5,6] Due to the challenges associated with fabricating highly defined surface topography at the nanoscale, most of this research has been performed on surfaces other than Ti, typically using lithography methods to produce nanopatterns in Si and then embossing these into soft polymers. Translating such nanopatterns to Ti and other metal implants is critically important, both to verify findings made on other material surfaces and to develop smart implants capable of controlling cell behavior in a predictable and precise manner.

In our previous work, we have focused on developing techniques that can produce highly defined nanopatterns on Ti surfaces, to perform studies of cell−topography interactions on a clinically relevant material, and develop implant surfaces with improved osseointegration properties. With our work on nanopatterning of Ti using nanoporous anodic alumina as anodization masks, we showed that it was possible to pattern bulk Ti surfaces with well-defined and tunable titania nanodots and nanopillars. These surfaces were used for mesenchymal stem cell studies which showed a distinct improved osteoinduction on low (e.g., 15 nm high) nanodots,[7,8] in line with data from other materials with similar nanopatterns.[9,10] One issue with the alumina through-mask anodization technique is that small amounts of Al or alumina could be present as residue on the surface, which could have adverse effects if released in vivo. It could also prove difficult to coat more complex shape surfaces with a layer of Al using a sputtering deposition method, and for creation of higher nanopillar features there may be an issue of mechanical stability, due to the formation of root-like attachments from the pillars to the substrate when using anodic alumina masks.[11]

To develop alternative techniques that are more suitable for nanopatterning of Ti implant surfaces with complex shapes, we have more recently used block copolymers (BCPs) as masks, or templates, for the anodization of Ti surfaces. Surface patterning using self-assembled BCPs has emerged as a promising technique to pattern large surface areas with nanolithographic precision in a cost-effective manner. BCPs consist of two covalently linked, chemically distinct polymers, which form

**Received:** September 13, 2012
**Accepted:** November 8, 2012
**Published:** November 8, 2012

   dx.doi.org/10.1021/am301987e | *ACS Appl. Mater. Interfaces* 2012, 4, 6354−6361

nanosized micelles when dissolved in a solvent that is selective to one of the blocks. The micellar solutions can be spin- or dip-coated onto most substrates which generates a thin polymer film with a self-assembled micellar arrangement. By utilizing the different properties of the two polymer blocks, such films can be used as templates for subsequent patterning of the substrate.[12−15] The high degree of order that can be achieved with BCP thin films results in a lithography-style nanopatterning technique which is easily applied to large surface areas and creates patterns which have previously been shown to stimulate osteogenesis on polymer surfaces.[16]

Poly(styrene-b-4-vinylpyridine) (PS-b-P4VP) has been widely used for BCP nanopatterning. The pyridine unit in the P4VP block becomes protonated in an acidic environment, which allows for easy incorporation of negatively charged precursors. Arrays of nanoparticles such as Au,[13,17] Pt and Pd,[14] and $TiO_2$[18] have been fabricated by incorporation of metallic salts followed by reduction to metallic or oxide nanoparticles. PS-b-P4VP templates have also been used as selective etch masks to create surfaces with nanopits.[12] Importantly, the dimensions and arrangement of the templates fabricated from BCPs can be finely controlled to create arrays of micelles with defined order and specific density.[15] The arrangement of the micelles can further be controlled to produce different geometries including nanodots, -lines,[19] and -rings.[20]

In this work, we demonstrate that PS-b-P4VP templates can be used to create well-defined and highly ordered arrays of titania nanodots and lines directly on bulk Ti surfaces via anodization. The dimensions of the nanodot patterns fabricated in this study are very similar to the 15 nm high nanodots we produced using other techniques and which were shown to stimulate an osteogenic differentiation of stem cells.[7,8] To characterize the detailed composition of the nanostructures and gain insight into the mechanism of feature formation, we have performed surface analyses at different points in the fabrication process. Finally, we show that the patterning technique can be used on nonplanar surfaces, i.e., Ti microbead specimens, which demonstrates that this technique can be used on actual Ti implants.

## 2. EXPERIMENTAL SECTION

Ti disks with 14 mm diameter were punched out of a 0.9 mm thick Ti sheet (ASTM grade 1) (Titanium Metals UK Ltd.). The disks were mechanically polished to a mirror finish. Ti microbeads were supplied and deposited onto polished Ti disks by Orchid Orthopedic Solutions, USA. The bead diameters ranged from 79.2 to 127 $\mu$m after deposition. A block copolymer with a molecular weight of 41.5-b-17.5 (PS-b-P4VP) $\times 10^3$ g mol$^{-1}$ was purchased from Polymer Source. The polymer was dissolved in a mixture of toluene and tetrahydrofuran (THF) (70/30% (v/v)) to a concentration of 0.5 wt % at 70 °C for 2 h and then allowed to cool to room temperature. To prepare thin films of polymer on the Ti substrates, the solutions were spin-coated at 2000 rpm for 60 s onto the Ti disks. The surfaces were then exposed to either THF or chloroform vapor for 3 h at room temperature in a sealed glass vessel. After 3 h, the samples were immediately removed from the vessel into air to allow quick drying of the polymer films. Anodization of the coated Ti substrates was performed in 0.01 M oxalic acid at room temperature with a two-electrode setup. A platinum strip was used as the cathode. The samples were immersed in the electrolyte for 60 s before the potential was applied. The electrolyte was magnetically stirred during the anodizations. The anodization potential was increased at a rate of 1 V s$^{-1}$ until 10 V was reached, and the samples were anodized for a total time of 60 s before the power supply was switched off. The samples were then immediately removed from the electrolyte and rinsed in distilled water and dried under a stream of air. To remove the polymer films, the samples were subjected to an oxygen plasma treatment at 100 W for 60 min, with a gas flow of 10 standard cubic centimeters per minute (SCCM) in a Femto plasma system (Diener Electronics). The surfaces were imaged using a field-emission scanning electron microscope (FE-SEM) (JEOL JSM 6330F) and atomic force microscopy (AFM) (Veeco Multimode with Quadrex Nanoscope 3D system).

Sputter depth profiling was performed using a ToF-SIMS IV (IONTOF GmbH, Münster, Germany) time-of-flight secondary ion mass spectrometer in a dual beam mode (i.e., 20 keV $C_{60}$ ion gun for sputtering and 25 keV Bi liquid metal ion gun for collecting spectra). A low energy electron flood gun was used for charge neutralization for all the measurements. The generated profiles were reconstructed from the raw data, and the characteristic secondary ions from the samples were selected to examine the surface composition in depth.

X-ray photoelectron spectroscopy (XPS) measurements were conducted using a Kratos Analytical Axis Ultra system with monochromatic Al $K_\alpha$ radiation ($h\nu$ = 1486.6 eV) at normal emission. A survey scan together with narrow scans of the C (1s), N (1s), O (1s), and Ti (2p) peaks were recorded close to the center of each sample at an X-ray source potential of 15 kV with 10 mA emission. Three separate areas were analyzed on each sample using electrons emitted normal to the surface. Charge compensation, using low energy electrons to flood the surface, was applied during all measurements. The acquired data were processed for both quantification and peak fitting using Casa XPS 2314 software. Surface elemental compositions were calculated from the peak areas using a linear background after correcting with Casa software sensitivity factors. The C (1s), N (1s), and O (1s) core-level peaks were fitted by Gaussian (70%)−Lorentzian (30%) functions with a Shirley background to measure each chemical state. The peak centers were fixed at the values given by Beamson and Briggs,[21] generally with scatters of 0.1 eV. A peak constrained was applied to above the main peak, of equal full width half-maximum (fwhm) to the main peak. Higher binding energy components were added if required. An energy calibration of 285 eV was applied to the main C (1s) peak for all samples.

Primary human mesenchymal stem cells (MSCs) (Promocell, Germany) (passage 2) were seeded at a density of 1 × $10^4$ cells/sample on Ti bead surfaces with and without superimposed nanopatterns and cultured for 3 days (for scanning electron microscopy; SEM) or 21 days (for immunostaining) in $\alpha$-MEM ($\alpha$-modified Eagle's medium (PAA Laboratories)) supplemented with 10% fetal bovine serum, 0.2 $\mu$g/mL of Fungizone, 67 U/mL of Penicillin, 66 $\mu$g/mL of streptomycin, and 1% (v/v) 200 mM L-glutamine in a humidified atmosphere of 5% $CO_2$. For the 21-day cultures, the culture medium was replaced with fresh medium three times per week. For immunostaining, cells were fixed after 21 days of culture in 3.8% formaldehyde in PBS (with 2% (w/v) sucrose) for 15 min at 37 °C. The fixative was removed, and cells were rinsed in PBS before permeabilization for 5 min in prechilled (4 °C) permeabilization buffer. The samples were blocked against nonspecific binding for 15 min at 37 °C in 1% (w/v) BSA (bovine serum albumin, Sigma) in PBS and incubated with primary goat antiosteocalcin antibody (clone V-19; 1:50 in 1% (w/v) BSA in PBS; Santa Cruz Biotechnology) for 1.5 h at 37 °C. The antibody was removed, and the cells were rinsed in PBST (three washes in 0.5% (v/v) Tween-20 in PBS for 5 min per wash) with gentle agitation. The samples were incubated with biotinylated secondary antigoat antibody (1:50 in 1% (w/v) BSA in PBS; Vector Laboratories, Burlingame, CA) and rhodamine phalloidin (1:50 in 1% (w/v) BSA in PBS; Invitrogen) for 1 h at 37 °C. The cells were rinsed three times in PBST and incubated with fluorescein-conjugated streptavidin for 30 min at 4 °C. The samples were rinsed another three times in PBST and mounted in mountant containing DAPI (Vector Laboratories, Burlingame, CA). For SEM, the culture medium was removed from the wells after 3 days of culture, and the samples were rinsed in prewarmed (37 °C) PBS. The cells were fixed in 1.5% (w/v) glutaraldehyde in 0.1 M sodium cacodylate for 1 h at 4 °C and then rinsed twice in 0.1 M sodium cacodylate. The samples were postfixed in osmium tetroxide for 1 h, rinsed three times in

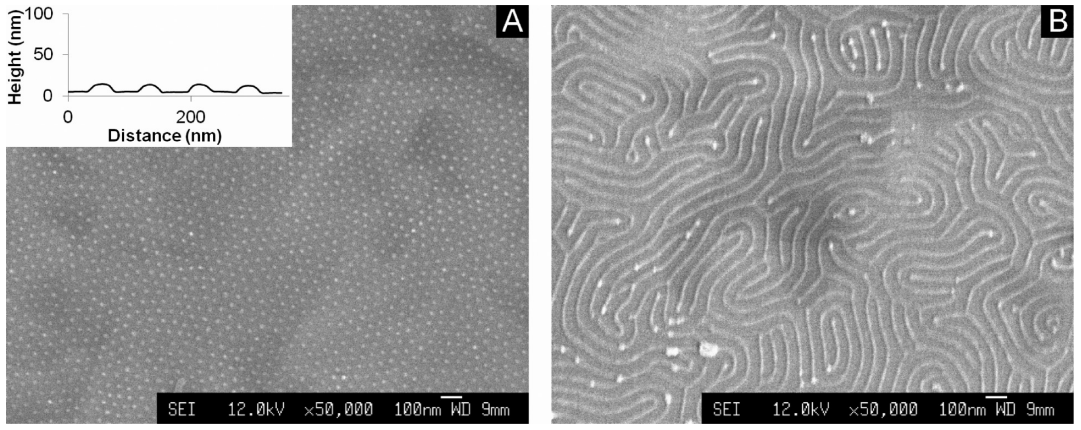


**Figure 1.** Typical nanopatterns on the Ti surface after anodization and removal of the polymer template, showing (A) a surface where the BCP template was solvent annealed in THF vapor and (B) a surface where the BCP template was solvent annealed in chloroform vapor. The inset in (A) shows a cross-section profile of the nanodots taken from AFM data which shows the approximate height of the nanofeatures.

distilled water, stained with 0.5% aqueous uranyl acetate for 1 h in the dark, washed twice in distilled water, and dehydrated in an ethanol series of 30%, 50%, 70%, 90%, and 100% ethanol, with the final dehydration step in hexamethyldisilazane (HMDS). The samples were sputter-coated with gold/palladium and viewed with SEM (JEOL 5600LV).

## 3. RESULTS AND DISCUSSION

**3.1. Nanopatterning of 2D Ti Surfaces.** Anodization of a Ti substrate results in oxide growth on the surface due to the field-assisted transportation of $Ti^{4+}$ and $O^{2-}/OH^{-}$ ions across the oxide. The anodization technique used in this work allowed for growth of an oxide that inherited the arrangement of the BCP template. Without the template, a smooth, uniform oxide was grown on the surface with no change in topography compared to the as-polished Ti substrates. Figure 1 shows a typical Ti surface patterned with titania nanodots after removal of the polymer template. The nanodot array shows an excellent arrangement and full surface coverage across the entire Ti disk, with the individual nanodots displaying a height of roughly 15 nm.

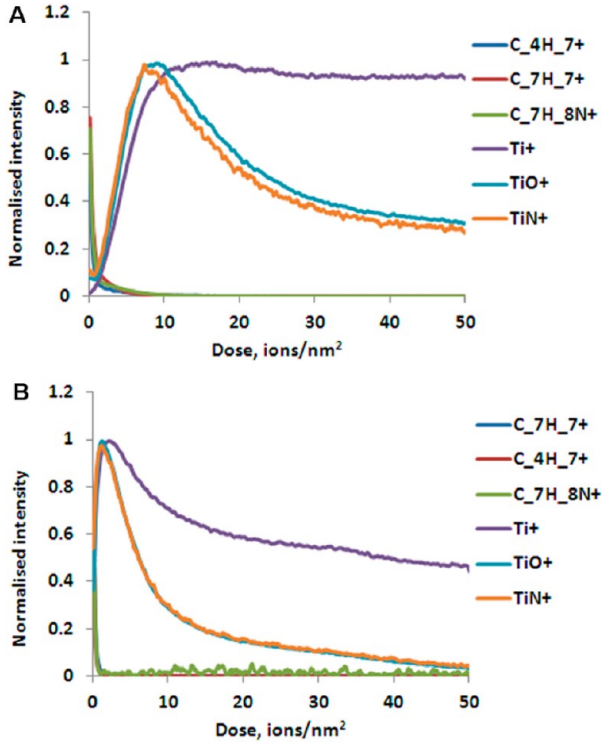


**Figure 2.** Positive secondary ion profiles as a function of sputtering time at different stages in the fabrication process. (A) As-anodized sample and (B) sample after BCP template removal.

The diameters of the nanodots produced with the BCP template in this work were 21 ± 4 nm, and the interdot distances were 30 ± 3 nm. The diameters and interdot distances are directly related to the micelle arrangement in the BCP mask and can be tuned by changing the molecular weight of the polymer blocks[15] or controlling the BCP spin- or dip-coating parameters.[22] The heights of the dots increased with the anodization potential and could thus be tuned independently of the other dimensions. We noticed that at potentials above 20 V the extensive oxide growth and gas generation at the anode destroyed the BCP film, and no titania nanodots were generated. A complete study of the dimensions and arrangements which are possible to achieve for the nanodot arrays is underway and will be reported separately.

Solvent annealing of the BCP template in chloroform vapor resulted in the arrangement of the BCP into a fingerprint-like pattern, rather than a hexagonal arrangement of nanodots. As can be seen, the line pattern was also directly translated to the titania nanopattern upon anodization and subsequent removal of the polymer template in oxygen plasma.

**3.2. Surface Chemical Characterization of a Nanopatterned Surface.** It is highly desirable to obtain the chemical information of each nanodot to elucidate surface chemical modifications that affect the nanopattern formation. However, currently no techniques with sufficient resolution to distinguish individual nanodots are available. We have used ToF-SIMS to characterize the anodized Ti surfaces both before and after removal of the BCP template to gain as much information about the formation process as possible. The SIMS depth profiles of the characteristic fragment ions are illustrated in Figure 2. For simplicity, the intensities of the characteristic secondary ions ($C_7H_7^+$ and $C_4H_7^+$ for PS, $C_7H_8N^+$ for P4VP, $TiO^+$ for $TiO_2$, and $Ti^+$ for Ti or $TiO_2$) were normalized and plotted on a linear scale. After anodization it is clear that the intensities of PS and P4VP decreased sharply in the low dose region (below 5 ions/nm$^2$). On the other hand, in Figure 2a the characteristic secondary ion intensities for $TiO_2$ ($TiO^+$) and

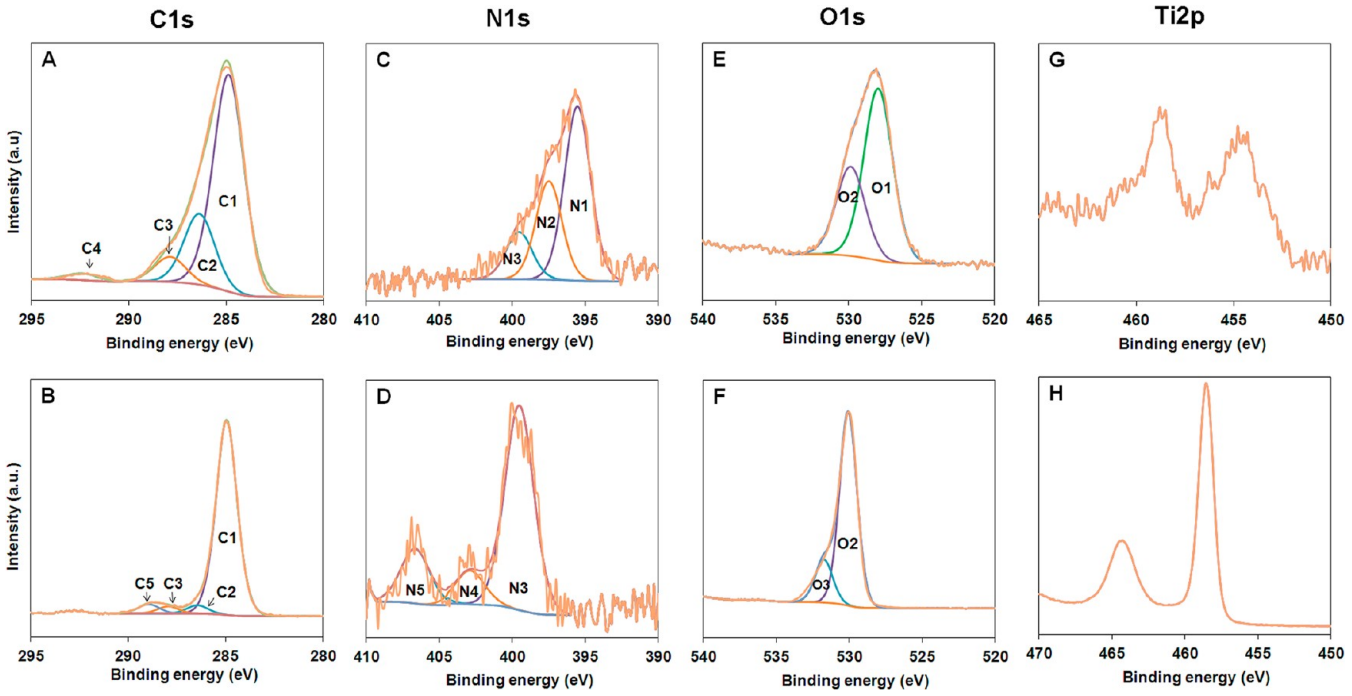


**Figure 3.** XPS narrow scan spectra for as-anodized sample (a) C (1s), (c) N (1s), (e) O (1s), and (g) Ti (2p) and after oxygen plasma etch (b) C (1s), (d) N (1s), (f) O (1s), and (h) Ti (2p). Each spectrum in (a)−(h) has been deconvolved by fitting to three Gaussian line shape functions. Components labeled in the spectra represent different bonding states in the chemical environment.

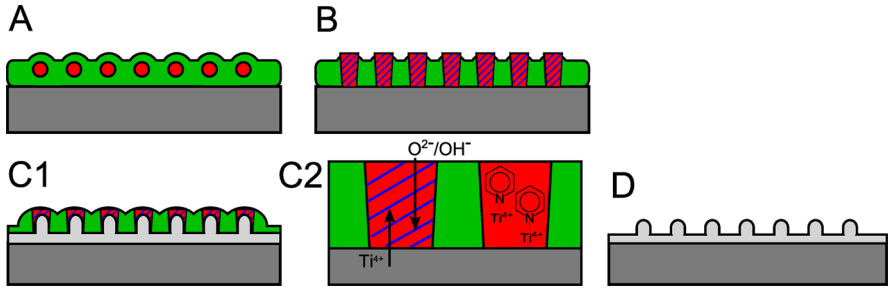


**Figure 4.** Schematic showing the processes during formation of the nanopatterns. Dark gray = Ti, red = P4VP, green = PS, and light gray = titania. (A) After spincoating the BCP onto the Ti substrate, a thin film of arranged micellar structures is formed. (B) When the sample is immersed in the electrolyte, the P4VP segments of the BCP are protonated and thus swell with electrolyte. (C1) During anodization anodic oxide grows within the P4VP segments at the same time as Ti ions interact directly with the P4VP. (C2) Enlarged view of the surface illustrating how $Ti^{4+}$ ions react with the P4VP. (D) Oxygen plasma treatment degrades the polymer template and oxidizes the surface further.

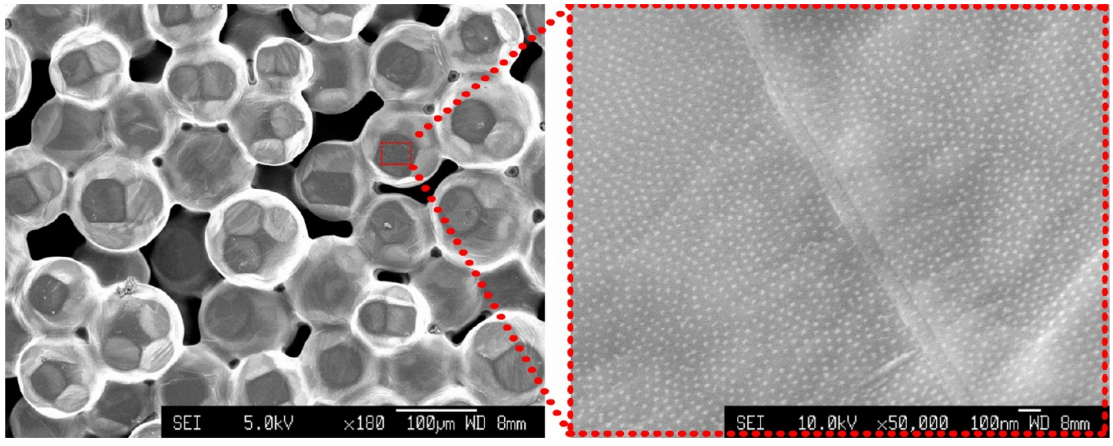


**Figure 5.** FE-SEM images of the nanopatterned Ti microbeads. The low magnification image shows the Ti microbeads which were dipcoated with the PS-b-P4VP polymer solution and subsequently anodized. At 50 000× magnification, the nanodot pattern is revealed, superimposed on top of the bead surfaces. The nanodot arrays were equivalent to those formed on planar Ti disks.


dx.doi.org/10.1021/am301987e | ACS Appl. Mater. Interfaces 2012, 4, 6354−6361

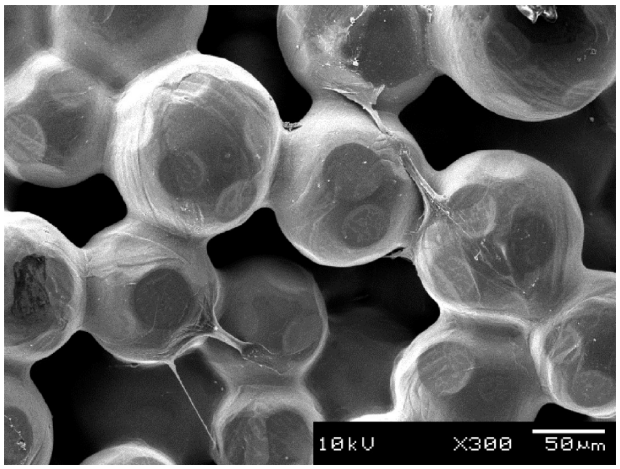


**Figure 6.** MSCs cultured for 3 days on Ti microbeads that also had a superimposed nanopattern produced by anodization with a BCP template. Note that some cells spanned between the microbeads.

TiN ($TiN^+$) increased steadily until reaching the maximum at ~6.8 ions/$nm^2$. This might suggest an interaction between Ti from the substrate and N in the P4VP domain. After ~10 ions/$nm^2$ dose, the entire film was etched through, as evidenced by the steady state of the Ti signal. In contrast, as shown in Figure 2b, there were almost no intensities from P4VP or PS on the top surface for the sample after removal of the polymer template by plasma treatment, and the interface was reached at ~0.7 ions/$nm^2$. Meanwhile, $TiO^+$ and $Ti^+$ secondary ion intensities increased monotonically up to the maximum and then decayed slowly. Also, after oxygen plasma treatment there appeared to be a significant amount of TiN at the surface. Although SIMS is a means of characterizing the average surface and not the individual nanodots, nevertheless, the results shown here indicated that the final surface composition after processing contains $TiO_2$ and TiN.

The surface chemistry of the samples both before and after removal of the BCP template was further examined in more detail using XPS. The relative molar ratios of elements on the surface of the as-anodized sample in XPS analysis depth (excluding hydrogen) were 86.3% C, 2.5% N, 9.1% O, 0.9% Ti, and 1.2% Si, whereas for the sample after removal of the BCP template, values were 26.0% C, 1.0% N, 52.7% O, 17.5% Ti, and 2.8% Si. The standard deviation of XPS measurements was better than 1% for each sample over three acquisition areas. The great reduction of the C signal indicates that most of the polymer film was removed in the oxygen plasma treatment. The presence of the small Si signal could indicate contaminants from the glassware used for the anodization of the Ti surfaces.

Figure 3 shows high-resolution XPS spectra of C (1s), N (1s), O (1s), and Ti (2p) with peaks fitted to the spectra. The C (1s) core-level spectra obtained from the as-anodized sample (Figure 3a) were deconvolved into three main peaks located at 284.8 eV (C1), 286.4 eV (C2), and 287.9 eV (C3), respectively. The peak C1 is attributed to aromatic carbons in the polymer molecule overlayers and in a small part from the hydrocarbon contaminations adsorbed onto the surface. The peak C2 originates from carbons bonded to nitrogen or oxygen (i.e., the P4VP), and the peak C3 could stem from the C═O group. A small ″shake up″ peak at 292.2 eV (C4) is observed with binding energy 6 eV higher than the main C1 peak. ″Shake up″ satellites often occur in the presence of aromatic systems ($\pi-\pi^*$ transition). After removal of the polymer template, the ″shake up″ peak C4 is no longer present, indicating that the PS has degraded. C2 is still present after polymer removal, but the spectral area ratio of the C1 component to that of the C2 component increases after plasma etching, again indicating degradation of the polymer. The C (1s) spectrum in Figure 3b is very similar to what was seen previously when titania nanodots were produced on a Si substrate using a PS-b-P2VP template.[18] As discussed by Li et al.,[18] it is difficult to distinguish whether the C (1s) peaks are due to insufficient removal of polymer template or to hydrocarbon contaminants. The peak at 284.8 eV can be largely attributed to the carbon contaminants that will exist on the surface after exposure to air,[23] but insufficient removal of PS cannot be ruled out. A new peak appeared at 289.0 eV (C5, 4 eV greater binding energy than adventitious carbon) after oxygen plasma treatment, which is typical of carboxyl (O−C═O) bonding groups.[18]

The breadth and asymmetry of the N (1s) core-level XPS spectra prior to polymer removal indicate the presence of different bonding states. The broad peak around 396 eV was deconvolved into three peaks (Figure 3c), located at 395.5 eV (N1), 397.5 eV (N2), and 399.5 eV (N3), respectively. The

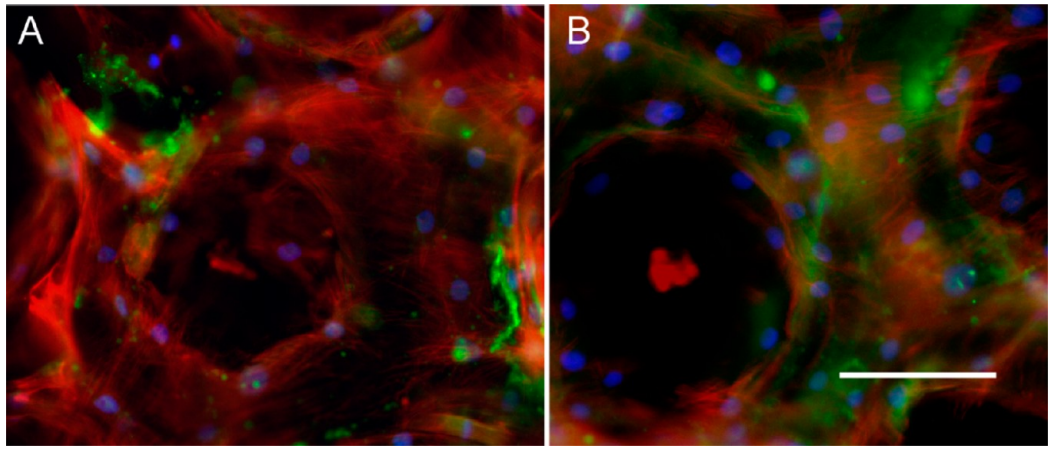


**Figure 7.** MSCs immunostained for the bone marker osteocalcin (green) and actin (red) after 21 days of culture on (A) Ti beads and (B) Ti beads with 15 nm nanodots superimposed. Note the considerable production of osteocalcin on both surfaces and the clustering of cells in the interbead spaces. Also note the almost uniform expression of osteocalcin across the entire cell population in (B). Scale bar = 100 $\mu$m.

peak N3 stems from the hydrogen-bonded imine moiety (−N=) of the P4VP pyridine rings.[24,25] The N2 peak can be attributed to TiN,[26] which is in accordance with the TiN peak seen for the Ti (2p) spectrum of the as-anodized sample and the SIMS results. The N1 peak was assigned as the incorporation of N into the $TiO_2$ lattice ($TiN_xO_y$),[27−29] but N1 could possibly relate to supersaturated $TiN_{1+x}$.[30] After removal of the polymer template in oxygen plasma, the N (1s) spectra looked different, with three peaks located at 399.5 eV (N3), 403.0 eV (N4), and 406.7 eV (N5) (Figure 3d). A peak around 400 eV is generally associated with chemisorbed N2 or N−N and N−C links,[26,31,32] and this peak has also been seen at low intensity for pure $TiO_2$ samples.[29] The N4 peak is, however, quite broad which suggests that there may be some P4VP remaining on the surface and possibly some contribution from TiN around 397 eV. The N4 and N5 peaks are associated with N−O compounds, typically reported in the 403−406 eV region.[33−35]

High-resolution XPS spectra of O (1s) are shown in Figure 3e and f. The binding energy of ∼529.9 eV (O2) corresponds to titanium oxide. There is a significant contribution to the broad main peak from PS and P4VP (O1) in Figure 3e. However, after BCP removal, the O2 peak in Figure 3f was narrower with no or little contribution from oxygen related to the polymers. There was also clear evidence of formation of Ti−N−O bonding at ∼531.7 eV (O3) after oxygen plasma treatment.

Figure 3g and h shows the Ti (2p) XPS spectra for the as-anodized and plasma-processed samples, respectively. Two peaks can be distinguished in the spectrum at 454.7 and 458.7 eV. The peak at 458.7 eV can be assigned to $Ti^{4+}$ states from $TiO_2$,[30,36] whereas the peak at 454.7 eV has previously been ascribed to TiN.[30] Since the polymer is covering the Ti substrate, these peaks are indicative of the Ti elements within the actual polymer template. After polymer removal, the Ti (2p) peaks showed a much higher intensity due to the XPS now probing the Ti substrate as well as the nanodots. Binding energies can be seen at 458.5 and 464.6 eV, representing Ti ($2p_{3/2}$) and Ti ($2p_{1/2}$), respectively.[37] There was no distinguished peak associated with TiN after removal of the polymer template, but it must be taken into account that the main contribution of the Ti (2p) signal comes from the Ti substrate and that deviations of the Ti (2p) signal inherited from the nanodots could be hard to detect. It is possible that the somewhat lower energy of 458.5 eV compared to the 458.8 eV previously reported for Ti ($2p_{3/2}$) is indicative of nitrogen incorporation into the lattice, replacing oxygen and resulting in the presence of $Ti^{3+}$ which gives a reduction in Ti ($2p_{3/2}$) energy.[38]

**3.3. Formation Mechanism of the Nanopatterned Surface.** Most nanopatterning techniques utilizing PS-b-P4VP and PS-b-P2VP BCPs have used the incorporation of negatively charged metallic precursors into the protonated P*x*VP domain ($x$ = 2, 4). Here, we show that by simply anodizing a valve metal substrate nanodots could be formed that inherited the P4VP arrangement from the BCP template. Figure 4 shows a schematic illustrating the formation mechanism of the titania nanodots. It is important to point out that the BCP template did not act as a porous mask during the anodization, which was the case for other BCP patterning techniques such as electrodeposition through PS-b-PMMA templates.[39] Instead the nanodots here formed within the P4VP segment of the BCP template. The formation of the titania pattern is mainly attributed to the selective incorporation of electrolyte into the P4VP domains, which allows for anodic growth in the P4VP. When the P4VP domains have been protonated, the electrolyte swells the hydrophilic P4VP, while the hydrophobic PS domain remains unaffected by the electrolyte.[40] This means that a reservoir of electrolyte is created within the P4VP block, and anodic oxidation can take place within the P4VP, as $Ti^{4+}$ ions are transported to the Ti/polymer interface. If a Ti substrate with BCP template was immersed into the electrolyte without applying a potential, no nanopattern was formed, which demonstrated the requirement for the anodization step in the formation of nanodots. The results from the surface analyses of the nanopatterned substrates clearly showed that the nanostructures were mainly titania, although the stoichiometry of the oxide is unknown. Apart from titania forming in the P4VP, the results from both the SIMS and XPS analyses showed that there was also formation of TiN and Ti−N−O compounds within the polymer template. This suggests that anodization was not the only factor responsible for the formation of nanodots. From previous studies, it is known that metal ions have a strong affinity to P4VP.[41,42] Therefore, it is highly likely that as Ti ions are ejected from the Ti substrate during anodization there will be a direct coordination between Ti ions and the pyridine in the P4VP block, effectively trapping Ti ions selectively within the P4VP domains of the BCP template. The SIMS results showed that there was TiN present after oxygen plasma processing, but it is likely that some of the TiN formed during anodization was oxidized during the plasma treatment, similarly to when Ti ions are loaded into P4VP from precursors and subsequently plasma treated.[43] Indeed, the XPS N (1s) spectra suggested that most of the nitrogen seems to have been replaced by oxygen. It has previously been suggested that during the oxidation of TiN atomic nitrogen is released and becomes chemisorbed on the surface,[26] which would agree with the findings in this report. During plasma treatment, the sample is heavily exposed to oxygen, which is likely to oxidize the Ti bound to N within the P4VP segment, effectively replacing and releasing the N. This would also explain the presence of the N5 and N6 peaks, which are associated with N−O compounds, typically reported in the 403−406 eV region,[33−35] presumably because the released N reacts with O during the oxygen plasma treatment. Judging by the intensity of the broad N (1s) peak in Figure 3c, which increases toward the lower energy part, it appears that most of the N is associated with Ti or $TiO_2$ after anodization. Also, the O (1s) spectra revealed the presence of Ti−O−N compounds. We cannot completely exclude the possibility that other events are partly responsible for the nanodot formation. Ti is known to form Ti oxalate complexes as the Ti surface is corroded in oxalic acid.[44] Such complexes may well exist within the P4VP segments.

**3.4. Nanopatterning of 3D Ti Surfaces.** To demonstrate the feasibility of using the current technique on surfaces with more complex shapes, BCP films were coated on Ti beads using dipcoating. The beads were deposited onto the same polished Ti disks as used above and had an average diameter of 100 $\mu$m. The beads were patterned using the same procedure as for the planar disks, resulting in the production of nanodot patterns on the surface of the beads, as shown in Figure 5. On the beaded surfaces, an excellent coverage of nanodots was observed, but it should be noted that it was difficult to obtain a thin BCP film in the deep crevices between the beads, and thus 100% coverage of nanodots was not achieved between the beads. Patterning of more complex shape surfaces such as the beads in Figure 5 is

crucial to translate well-defined nanopatterning techniques to actual Ti implant surfaces.

**3.5. In Vitro Studies.** With the nanopatterning technique presented in the current study, it is possible to study the influence of precise nanotopography on cells in vitro on clinically relevant Ti surfaces, especially in 3D, rather than drawing conclusions from nanopatterns on 2D model surfaces, which has often been the case. Figure 6 shows a SEM image of mesenchymal stem cells (MSCs) that had been cultured for 3 days on Ti beads patterned with nanodots (as shown in Figure 5). The cells were well spread on these surfaces and could sometimes be seen to span between microbeads. Figure 7 shows MSCs stained for the bone marker osteocalcin after 21 days of culture. There appeared to be a higher expression of osteocalcin in cells cultured on the nanopatterned beads, but more quantitative in vitro and in vivo studies are needed to demonstrate the precise effects of the superimposed nanodots.

## 4. CONCLUSIONS

To summarize, we have conducted detailed analyses of the nanopatterns formed on Ti surfaces using a novel patterning technique combining anodization with BCP templates. The nanopatterns formed consisted of titania and partly of TiN and other minor compositions due to a complex formation mechanism. We have further demonstrated that this patterning technique can be used not only on planar (flat disk) Ti surfaces but also on nonplanar Ti surfaces (microbeads), with no or little change in the nanopatterns compared to those formed on flat disk substrates. This paves a way for clinical translation, by facilitating the production of defined nanotopographies on real Ti implants for orthopedic, dental, and other biomedical applications.

## AUTHOR INFORMATION

### Corresponding Author

*E-mail: terje.sjostrom@bristol.ac.uk.

### Notes

The authors declare no competing financial interest.

## ACKNOWLEDGMENTS

The research presented in the above study was funded by the EPSRC through grant numbers EP/G049076/1 and EP/G048703/1. Orchid Orthopaedic Solutions (USA) is kindly acknowledged for supplying the titanium beads, and the authors would like to thank Mrs. Margaret Mullin (EM Unit, University of Glasgow) for assistance with sample preparation for SEM.

## REFERENCES

(1) Hulander, M.; Lundgren, A.; Berglin, M.; Ohrlander, M.; Lausmaa, J.; Elwing, H. *Int. J. Nanomed.* **2011**, *6*, 2653−2666.
(2) McMurray, R. J.; Gadegaard, N.; Tsimbouri, P. M.; Burgess, K. V.; McNamara, L. E.; Tare, R.; Murawski, K.; Kingham, E.; Oreffo, R. O. C.; Dalby, M. J. *Nat. Mater.* **2011**, *10*, 637−644.
(3) Xu, L.-C.; Siedlecki, C. A. *Acta Biomater.* **2012**, *8*, 72−81.
(4) Palmquist, A.; Grandfield, K.; Norlindh, B.; Mattsson, T.; Branemark, R.; Thomsen, P. *J. R. Soc. Interface* **2012**, *9*, 396−400.
(5) Park, J.; Bauer, S.; von der Mark, K.; Schmuki, P. *Nano Lett.* **2007**, *7*, 1686−1691.
(6) Huang, J.; Grater, S. V.; Corbellinl, F.; Rinck, S.; Bock, E.; Kemkemer, R.; Kessler, H.; Ding, J.; Spatz, J. P. *Nano Lett.* **2009**, *9*, 1111−1116.
(7) Sjostrom, T.; Dalby, M. J.; Hart, A.; Tare, R.; Oreffo, R. O. C.; Su, B. *Acta Biomater.* **2009**, *5*, 1433−1441.
(8) McNamara, L. E.; Sjoestroem, T.; Burgess, K. E. V.; Kim, J. J. W.; Liu, E.; Gordonov, S.; Moghe, P. V.; Meek, R. M. D.; Oreffo, R. O. C.; Su, B.; Dalby, M. J. *Biomaterials* **2011**, *32*, 7403−7410.
(9) Lim, J. Y.; Hansen, J. C.; Siedlecki, C. A.; Runt, J.; Donahue, H. J. *J. R. Soc. Interface* **2005**, *2*, 97−108.
(10) Dalby, M. J.; Giannaras, D.; Riehle, M. O.; Gadegaard, N.; Affrossman, S.; Curtis, A. S. G. *Biomaterials* **2004**, *25*, 77−83.
(11) Sjoestroem, T.; Fox, N.; Su, B. *Electrochim. Acta* **2010**, *56*, 203−210.
(12) Qiao, Y. H.; Wang, D.; Buriak, J. M. *Nano Lett.* **2007**, *7*, 464−469.
(13) Aizawa, M.; Buriak, J. M. *J. Am. Chem. Soc.* **2005**, *127*, 8932−8933.
(14) Chai, J.; Wang, D.; Fan, X. N.; Buriak, J. M. *Nat. Nanotechnol.* **2007**, *2*, 500−506.
(15) Spatz, J. P.; Eibeck, P.; Mossmer, S.; Moller, M.; Herzog, T.; Ziemann, P. *Adv. Mater.* **1998**, *10*, 849−852.
(16) Maclaine, S. E.; Gadhari, N.; Pugin, R.; Meek, R. M. D.; Liley, M.; Dalby, M. J. *J. Orthop. Res.* **2012**, *30*, 1190−1197.
(17) Spatz, J. P.; Mossmer, S.; Hartmann, C.; Moller, M.; Herzog, T.; Krieger, M.; Boyen, H. G.; Ziemann, P.; Kabius, B. *Langmuir* **2000**, *16*, 407−415.
(18) Li, X.; Lau, K. H. A.; Kim, D. H.; Knoll, W. *Langmuir* **2005**, *21*, 5212−5217.
(19) Kim, T. H.; Huh, J.; Hwang, J.; Kim, H. C.; Kim, S. H.; Sohn, B. H.; Park, C. *Macromolecules* **2009**, *42*, 6688−6697.
(20) Zu, X.; Hu, X.; Lyon, L. A.; Deng, Y. *Chem. Commun.* **2010**, *46*, 7927−7929.
(21) Beamson, G. B., D. In *High Resolution XPS of Organic Polymers − The Scienta ESCA300 Database*; Wiley: Chichester, 1992; pp 1−295.
(22) Krishnamoorthy, S.; Pugin, R.; Brugger, J.; Heinzelmann, H.; Hinderling, C. *Adv. Funct. Mater.* **2006**, *16*, 1469−1475.
(23) Yuwono, A. H.; Zhang, Y.; Wang, J.; Zhang, X. H.; Fan, H.; Ji, W. *Chem. Mater.* **2006**, *18*, 5876−5889.
(24) Cen, L.; Neoh, K. G.; Kang, E. T. *Langmuir* **2003**, *19*, 10295−10303.
(25) Yang, G. H.; Kang, E. T.; Neoh, K. G.; Zhang, Y.; Tan, K. L. *Langmuir* **2001**, *17*, 211−218.
(26) Saha, N. C.; Tompkins, H. G. *J. Appl. Phys.* **1992**, *72*, 3072−3079.
(27) Miao, L.; Tanemura, S.; Watanabe, H.; Mori, Y.; Kaneko, K.; Toh, S. *J. Cryst. Growth* **2004**, *260*, 118−124.
(28) Morikawa, T.; Asahi, R.; Ohwaki, T.; Aoki, K.; Taga, Y. *Jpn. J. Appl. Phys., Part 2* **2001**, *40*, L561−L563.
(29) Asahi, R.; Morikawa, T.; Ohwaki, T.; Aoki, K.; Taga, Y. *Science* **2001**, *293*, 269−271.
(30) Bertoti, I.; Mohai, M.; Sullivan, J. L.; Saied, S. O. *Appl. Surf. Sci.* **1995**, *84*, 357−371.
(31) Kim, D.; Tsuchiya, H.; Fujimoto, S.; Schmidt-Stein, F.; Schmuki, P. *J. Solid State Electrochem.* **2012**, *16*, 89−92.
(32) Raut, N. C.; Mathews, T.; Rajagopalan, S.; Rao, R. V. S.; Dash, S.; Tyagi, A. K. *Solid State Commun.* **2011**, *151*, 245−249.
(33) Rosenberger, L.; Baird, R.; McCullen, E.; Auner, G.; Shreve, G. *Surf. Interface Anal.* **2008**, *40*, 1254−1261.
(34) Shi, J.-H.; Yang, B.-X.; Goh, S. H. *Eur. Polym. J.* **2009**, *45*, 1002−1008.
(35) Mitoraj, D.; Kisch, H. *Angew. Chem., Int. Ed.* **2008**, *47*, 9975−9978.
(36) Luca, D.; Hsu, L. S. *J. Optoelectron. Adv. Mater.* **2003**, *5*, 835−840.
(37) Chu, C. L.; Wang, R. M.; Hu, T.; Yin, L. H.; Pu, Y. P.; Lin, P. H.; Dong, Y. S.; Guo, C.; Chung, C. Y.; Yeung, K. W. K.; Chu, P. K. *J. Mater. Sci.: Mater. Med.* **2009**, *20*, 223−228.
(38) Wang, D.-H.; Jia, L.; Wu, X.-L.; Lu, L.-Q.; Xu, A.-W. *Nanoscale* **2012**, *4*, 576−584.
(39) Thurn-Albrecht, T.; Schotter, J.; Kastle, C. A.; Emley, N.; Shibauchi, T.; Krusin-Elbaum, L.; Guarini, K.; Black, C. T.; Tuominen, M. T.; Russell, T. P. *Science* **2000**, *290*, 2126−2129.

(40) Pietsch, T.; Gindy, N.; Fahmi, A. *Soft Matter* **2009**, *5*, 2188−2197.
(41) Krenek, R.; Stamm, M.; Cimrova, V. *J. Appl. Phys.* **2008**, *103*, 044306−1−044306−16.
(42) Gowd, E. B.; Nandan, B.; Bigall, N. C.; Eychmueller, A.; Formanek, P.; Stamm, M. *Polymer* **2010**, *51*, 2661−2667.
(43) Weng, C. C.; Hsu, K. F.; Wei, K. H. *Chem. Mater.* **2004**, *16*, 4080−4086.
(44) El-Mahdy, G. A. *Corrosion* **2007**, *63*, 299−306.